Sonoelastographic imaging of interference patterns for estimation of shear velocity distribution in biomaterials

Zhe Wu[a] and Kenneth Hoyt
ECE Department, University of Rochester, Hopeman Building 204, Rochester, New York 14627-0126

Deborah J. Rubens
Department of Radiology, University of Rochester, Rochester, New York 14627

Kevin J. Parker
ECE Department, University of Rochester, Hopeman Building 204, Rochester, New York 14627-0126

(Received 29 September 2005; revised 17 April 2006; accepted 18 April 2006)

The authors have recently demonstrated the shear wave interference patterns created by two coherent vibration sources imaged with the vibration sonoelastography technique. If the two sources vibrate at slightly different frequencies ω and $\omega+\Delta\omega$, respectively, the interference patterns move at an apparent velocity of $(\Delta\omega/2\omega)*v_{\text{shear}}$, where v_{shear} is the shear wave speed. We name the moving interference patterns "crawling waves." In this paper, we extend the techniques to inspect biomaterials with nonuniform stiffness distributions. A relationship between the local crawling wave speed and the local shear wave velocity is derived. In addition, a modified technique is proposed whereby only one shear wave source propagates shear waves into the medium at the frequency ω. The ultrasound probe is externally vibrated at the frequency $\omega-\Delta\omega$. The resulting field estimated by the ultrasound (US) scanner is proven to be an exact representation of the propagating shear wave field. The authors name the apparent wave motion "holography waves." Real-time video sequences of both types of waves are acquired on various inhomogeneous elastic media. The distribution of the crawling/holographic wave speeds are estimated. The estimated wave speeds correlate with the stiffness distributions. © *2006 Acoustical Society of America.* [DOI: 10.1121/1.2203594]

PACS number(s): 43.80.Jz [CCC] Pages: 535–545

I. INTRODUCTION

It is well known that changes in tissue mechanical properties are possible disease markers. In modern medicine, digital palpation is a routine screening method in physical examinations. In recognizing the significance, many scientists and researchers are developing various imaging modalities to visualize one or more parameters of the tissue mechanical properties qualitatively. Among many material properties parameters, shear wave propagation speed (and/or wavelength) has many researchers' interests, because the shear wave speed is closely related to shear modulus of elastic media (Love 1944). Parker and Lerner (1992) related shear wave speed to the production of eigenmodes in homogeneous biological materials. Yamakoshi *et al.* (1990) estimated both the vibration amplitude and phase due to external excitation with ultrasonic probing beams. Levinson *et al.* (1995) measured shear wave propagation speed in skeletal muscle *in vivo* with phase based ultrasonic techniques. Muthupillai *et al.* (1995) visualized the physical response of a material to harmonic mechanical excitation with phase encoded magnetic resonance imaging (MRI). Sandrin *et al.* (1999) developed an ultrafast imaging system (up to 10 000 frames/s), which is able to image the propagation of the low-frequency transient shear waves. Vibration displacements are measured using cross correlation of the ultrasonic signals (Sandrin *et al.* 1999). Dutt *et al.* (2000) measured small cyclic displacements (submicrometer level) caused by propagating shear waves in tissuelike media with a phase-based ultrasound method. Jenkyn and Ehman (2003) estimated the shear wave wavelength in skeletal muscles with magnetic resonance elastography (MRE). Shear wave wavelengths were found to increase with increasing tissue stiffness and increasing tissue tension (Jenkyn and Ehman 2003).

II. THEORY

A. Sonoelastography

The methods we propose are based on an ultrasonic imaging modality called sonoelastography (Lerner *et al.* 1988). Sonoelastography estimates the peak displacements of particle motion under audio frequency excitations by analyzing the power spectrum variance of the U.S. echoes, which is proportional to the local vibration amplitude (Huang *et al.* 1990, Taylor *et al.* 2000). Vibration fields are then mapped to a commercial ultrasound scanner's screen. Since this technique utilizes the existing Doppler hardware on most modern U.S. scanners, the frame rate of sonoelastography is as high as other Doppler modalities. Regions where the vibration amplitude is low are displayed as dark green, while regions with high vibration are displayed as bright green. Unless additional phase estimators are employed (Huang *et al.* 1992), sonoelastography ignores the phase information of

[a]Electronic address: wuzhe@ece.rochester.edu

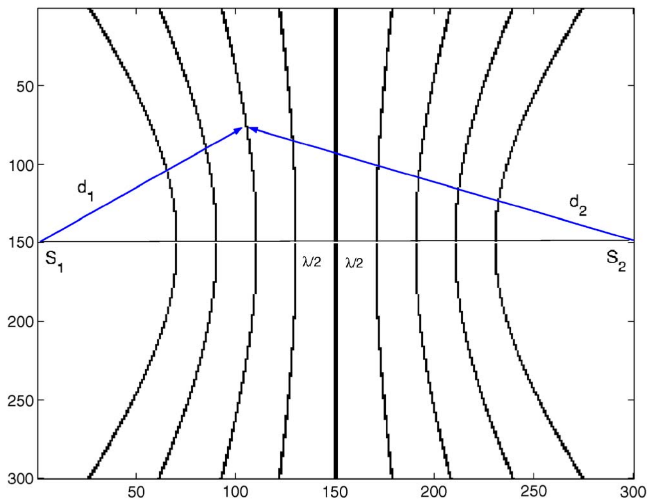

FIG. 1. S_1 and S_2 are the shear wave sources. If they vibrate in phase at equal amplitude, the antinodes lines of the interference pattern can be represented by a family of hyperbolas where $|d_1-d_2|=n\lambda$, n being integer numbers. Along the line S_1S_2, the spacing between the antinode lines is equal to $\lambda/2$.

shear wave propagations. Sonoelastography has been applied to visualize shear wave transducers' beam patterns or interference patterns (Wu *et al.* 2002).

B. Static shear wave interference patterns (a review)

As we reported in the previous paper (Wu *et al.* 2004), coherent shear wave sources create shear wave interference patterns in the media and the patterns can be visualized by sonoelastography in real time. Assuming the medium is homogeneous and isotropic, the phase of an arbitrary point in the vibration field is proportional to the distance between this point and the wave source

$$\phi = kd, \tag{1}$$

where k is the shear wave number and d is the distance from the field point to the wave source. In such a medium of infinite size, if there exists two coherent shear wave sources, then interference patterns appear. If the two sources are in phase, the antinode lines, which correspond to high vibration amplitudes, reside in such locations that the distance d_1 and d_2 have constant differences which equal integer multiple of the shear wavelength. The definition of d_1 and d_2 is depicted in Fig. 1,

$$|\phi_1 - \phi_2| = 2n\pi$$

$$|kd_1 - kd_2| = 2n\pi$$

$$|d_1 - d_2| = n\lambda \tag{2}$$

where n is an integer.

In other words, the interference patterns can be represented as a family of hyperbolas (Fig. 1). Assuming the distance between the two wave sources is D, the function of the family of hyperbolas can be expressed as

$$\frac{x^2}{a^2} - \frac{y^2}{b^2} = 1$$

where $a = \frac{n\lambda}{2}$

$$\text{and } b^2 = \left(\frac{D}{2}\right)^2 - a^2 \tag{3}$$

If we set $y=0$, Eq. (3) yields

$$x = \pm \frac{n\lambda}{2}. \tag{4}$$

Equation (4) states that along the central axis, the distance between the x intercepts of this family of hyperbolas equals half of the shear wave wavelength. If the two shear wave sources are far away compared to the size of the field of view, the family of hyperbolas can be approximated as parallel lines. This is equivalent to assuming the waves from each source are plane waves.

C. Moving shear wave interference patterns (a review)

Again in homogeneous and isotropic media, if one of the two sources vibrates at the frequency ω and the other source vibrates at $\omega+\Delta\omega$, where $\Delta\omega \ll \omega$, the interference patterns no longer remain static. They move toward the source with the lower frequency. Throughout the rest of this paper, we assume the two sources vibrate in such a fashion unless otherwise stated. This is referred to as the frequency difference condition. Following the derivation in the previous section, the location of the patterns should follow the equation:

$$|kd_1 - (kd_2 + \Delta\omega t)| = 2n\pi. \tag{5}$$

Following the same derivation in Eq. (4), the family of hyperbolas intercept the x axis at

$$x = \pm \frac{n\lambda}{2} + \frac{\Delta\omega \cdot \omega}{2\omega \cdot k} t$$

$$x = \pm \frac{n\lambda}{2} + \frac{\Delta\omega}{2\omega} t v_{\text{shear}}. \tag{6}$$

Therefore, the x intercepts of the hyperbolas move at the speed of $(\Delta\omega)/(2\omega)v_{\text{shear}}$. If we further assume the waves from each source are plane waves, then the whole interference pattern moves at this speed. We name the interference pattern motion crawling waves. Accordingly, the interference fringes are named crawling wave fronts; the spacing between the interference fringes is the crawling wavelength.

D. Crawling wave in inhomogeneous media

One important element to generalize the above results into elastic property estimation of inhomogeneous media is to understand the crawling wave's behavior *locally*. Despite the fact that the interference fringes' locations depend on the path integral of phase from each source, the following discussion proves that the crawling wave velocity depends solely on the local property [to a certain approximation in the two-dimensional (2D) case].

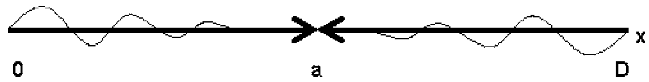

FIG. 2. Two shear wave sources are at 0 and D, respectively.

1. One-dimensional problem

We start with the one-dimensional problem. As depicted by Fig. 2, there are two wave sources at 0 and D, respectively. Without the loss of generality, we assume the two sources are in phase at the initial time ($t=0$). One source has frequency ω and the other source has frequency $\omega+\Delta\omega$. As we stated in the previous section, the locations of the antinodes are dependent on time. For instance, if one antinode resides at a, at $t=T, T>0$, we can write an equation on the phase relation

$$\int_0^a k(x)dx = \int_D^a -k(x)dx + \Delta\omega t + 2n\pi, \tag{7}$$

where $k(x)$ is the local wave number of the shear wave and $-k(x)$ indicates the wave propagation at the negative direction.

Now we take the derivative relative to a, on both sides of Eq. (7)

$$k(x) = -k(x) + \frac{d}{da}\Delta\omega t = -k(x) + \Delta\omega\frac{dt}{da}. \tag{8}$$

Note that da/dt is the apparent velocity of the antinode v_{pattern}

$$v_{\mathrm{pattern}}(x) = \frac{\Delta\omega}{2k(x)} = \frac{\Delta\omega}{2\omega}v_{\mathrm{shear}}(x). \tag{9}$$

This proves that the speed of the interference motion is directly proportional to the local velocity of the shear waves. The ratio of the apparent velocity to the local shear velocity is $\Delta\omega/2\omega$.

According to the equation above, there are clearly some advantages to investigating the interference patterns motions. First, this technique virtually slows down the shear wave propagation by a controllable factor $\Delta\omega/2\omega$. This enables available U.S. systems to visualize the wave propagation. Second, the local shear wave velocity can be recovered once the pattern motion is analyzed.

2. Two-dimensional problem

One of the challenges to generalize the previous derivation into two-dimensional (2D) domain is that in generalized media, according to Fermat's principle, waves do not necessarily travel along straight lines. Therefore, the phase at any particular field point is a complicated line integral over a curve. However, we can consider an infinitesimal region where the material property is approximately homogeneous and all waves can be approximated as plane waves (Greenleaf *et al.* 2003). A geometrical analysis in such infinitesimal regions is given in Appendix A. We find in the 2D case, in addition to the local shear speed, the crawling wave speed is also related to the angle between the wave fronts from each source

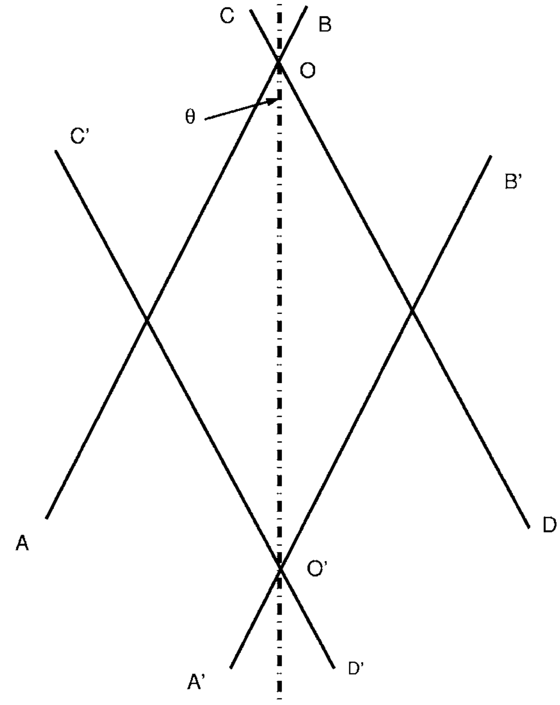

FIG. 3. The geometry of shear wave wave fronts in an infinitesimal region. The shear wave sources (not shown) are vibrating at the same frequency. At $t=0$, AB is the wave front from source 1 and CD is the wave front from source 2; at $t=T$, $A'B'$ is the wave front from source 1 and $C'D'$ is the wave front from source 2.

$$v_{\mathrm{pattern}} = \frac{\Delta\omega}{2\omega}\cdot\frac{v_{\mathrm{shear}}}{\cos\left(\frac{\theta}{2}\right)}, \tag{10}$$

where θ is defined in Fig. 3.

If the region of interest (ROI) is in the far field of both the two shear wave sources, $\theta/2$ is a small quantity, and $\cos(\frac{\theta}{2})$ is close to 1. The case where the lesion size is larger than the shear wave wavelength is out of the scope of this paper but discussed in detail by Ji and Mclaughlin (2004).

When $\cos(\frac{\theta}{2})$ is close to 1

$$v_{\mathrm{pattern}} \approx \frac{\Delta\omega}{2\omega}\cdot v_{\mathrm{shear}}. \tag{11}$$

E. Holographic wave

The technique of crawling waves requires two coherent shear wave sources from the opposing two sides of the region of interest. Sometimes, this particular configuration is not easy to achieve in practice. Meanwhile, as discussed previously, the interference fringes closely approximate the shear wave wave fronts only when the perturbation of the elasticity in the medium is small. The application of these techniques is thus limited. To overcome this drawback and to visualize the *exact* wave fronts of shear waves, another technique is proposed, which only requires one shear wave source touching the testing samples.

In this technique, the ultrasound probe, which is the observer and the frame of reference, is vibrated while the shear wave source transmits the waves. As Fig. 4 depicts, the shear

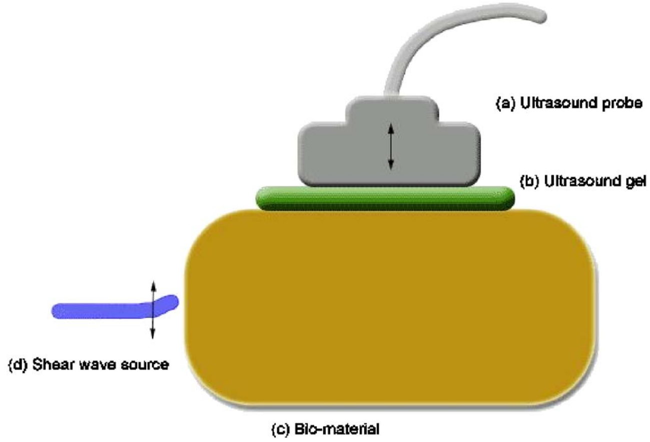

FIG. 4. Shear wave holography setup: (a) the ultrasound probe is externally vibrated at the frequency $\omega - \Delta\omega$, where $\Delta\omega \ll \omega$; (b) the thick layer of liquid ultrasound gel isolates the probe motion so it does not penetrate into the elastic material; (c) the elastic material; (d) the shear wave source vibrating at the frequency ω. The black arrows indicate the motion direction.

wave source vibrates at the frequency ω. Induced by the shear wave source, each particle in the medium oscillates at the same frequency with a spatially dependent phase term. The derivative of the phase term is the velocity of the shear wave. Assuming the shear wave source is stationary and harmonic, the vibration field can be written as $f(x)$ where $f(x)$ is a function of the 2D spatial variable x. In addition, we allow the spatial dependent part of the wave equation to be any arbitrary function of x subject to the wave equation. In other words, we do not require the wave to take any particular form (such as plain wave, spherical wave, etc.). Let the spatial dependent term be $s(x)$ [in the plain wave case, $s(x) = k \cdot x$], the vibration field can be written as

$$U(x,t) = f(x) * \exp\{i[\omega t - s(x)]\}. \tag{12}$$

The wave fronts of $U(x,t)$ are determined by assigning $[\omega t - s(x)]$ to a constant

$$\omega t - s(x) = \phi,$$

$$\omega t = s(x) - \phi,$$

where ϕ is a constant phase.

Taking the time derivatives on both sides

$$\omega = \text{grad}[s(x)] * \frac{dx}{dt}. \tag{13}$$

Multiplying both sides by $1/|\text{grad } s|$

$$\frac{\omega}{|\text{grad}(s)|} = \vec{n} * \frac{dx}{dt}, \tag{14}$$

where $\vec{n}$ is the unit vector normal to the wave front and it is along the direction of shear wave propagation. Therefore

$$\upsilon_s = \vec{n} * \frac{dx}{dt} = \frac{\omega}{|\text{grad}(s)|}, \tag{15}$$

where υ_s is the shear wave phase velocity and $|\text{grad}(s)|$ is the gradient of $s(x)$.

While transmitting and receiving ultrasound signals, the ultrasound probe is also externally vibrated. The ultrasound probe is carefully positioned above the biomaterial without touching it. A thick layer of the ultrasound gel is applied to acoustically connect the probe and the biomaterial. In this setup, the ultrasound probe does *not* propagate shear waves into the biomaterial. Since the liquid ultrasound gel does not support shear waves, it isolates the ultrasound probe motion from penetrating into the medium.

Because the ultrasound probe is the observer and thus the frame of reference, the particle motion relative to the ultrasound probe is estimated by the sonoelastography algorithm. Therefore the *estimated* shear wave field is modulated by the probe motion. Instead of the shear wave source frequency ω the ultrasound probe is tuned to vibrate at a slight different frequency $\omega - \Delta\omega$, where $\Delta\omega \ll \omega$. Therefore, the motion of the ultrasound probe is

$$R(t) = A * \exp[i(\omega - \Delta\omega)t], \tag{16}$$

where A is a constant.

Hence the vibration field relative to the ultrasound probe is

$$P(x,t) = U(x,t) - R(t) = f(x) * \exp\{i[\omega t - s(x)]\} - A * \exp[i(\omega - \Delta\omega)t]. \tag{17}$$

The square of $P(x,t)$'s envelope is

$$\begin{aligned} |P(x,t)|^2 &= P * P^* = [U(x,t) - R(t)] * [U(x,t)^* - R(t)^*] \\ &= (f(x) * \exp\{i[\omega t - s(x)]\} - A * \exp[i(\omega \\ &\quad - \Delta\omega)t]) * (f(x) * \exp\{-i[\omega t - s(x)]\} \\ &\quad - A * \exp[-i(\omega - \Delta\omega)t]) = f(x)^2 + A^2 \\ &\quad - A \cdot f(x)\exp[i\Delta\omega t - is(x)] - A \cdot f(x) \\ &\quad \times \exp[-i\Delta\omega t + is(x)] = f(x)^2 + A^2 \\ &\quad - 2A \cdot f(x)\cos[\Delta\omega t - s(x)], \end{aligned} \tag{18}$$

where P^* is the complex conjugate of P.

We name $|P^2(x,t)|$ the holographic wave. Similar to Eq. (15), taking $\Delta\omega$ as the equivalent frequency and the velocity of the holographic wave is

$$\upsilon_m = \frac{\Delta\omega}{|\text{grad}(s)|}. \tag{19}$$

Comparing Eq. (19) with Eq. (15), it is clear that

$$\upsilon_m = \frac{\Delta\omega}{\omega} \cdot \upsilon_s. \tag{20}$$

Also notice that because the US probe motion is only a function of time, the mechanical modulation does not interfere with the spatial component of Eq. (12), i.e., $s(x)$. Therefore the exact shear wave appearance is preserved. Apart from a dc shift in the amplitude and a change in the velocity, the shear wave propagation is exactly represented by the holographic wave. With the proposed technique, the shear wave can be slowed down by an arbitrary yet controllable factor $\Delta\omega/\omega$. Therefore, with the mechanical modulation, the phase

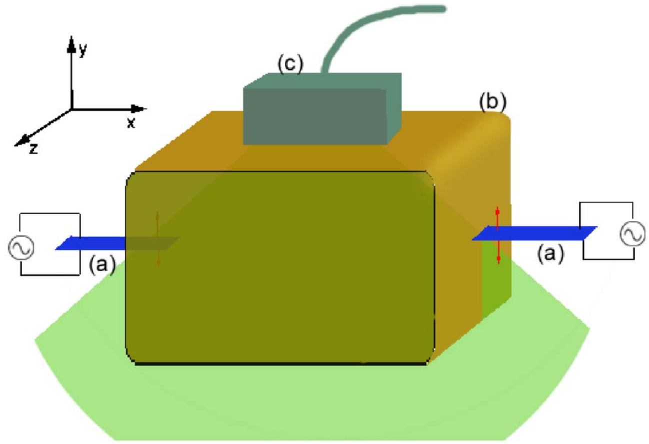

FIG. 5. Schematic drawing of the experiment setup. Two bimorphs (a) are in close contact with the phantom (b). The arrows indicate the motion vectors of the tips of the bimorphs. The sector shape depicts the imaging plane of the ultrasound probe (c).

of the shear waves is recovered and the speed is reduced to be studied by the ordinary US scanners with sonoelastography modifications.

F. Pattern motion speed reconstruction

The interference pattern motion velocity may be reconstructed with many existing wave motion inversion techniques such as discussed in Dutt *et al.* (1997), Catheline *et al.* (1999), Oliphant *et al.* (2000), Bishop *et al.* (2000), and Braun *et al.* (2001). In this article, the local spatial frequency estimator (LFE) is selected to demonstrate the feasibility to apply the crawling wave and holographic wave techniques as an elasticity imaging technique. The local spatial frequency is obtained by passing the images through a bank of 2D lognormal filters and averaging the outputs, as originally proposed by Knutsson *et al.* (1994) and modified by Manduca *et al.* (1996) to be employed in MRE estimations as a Helmholtz inversion technique. Note the local shear wave speed is inversely proportional to the local spatial frequency k_l: $v_{\text{crawl}}=\omega/k_l$. Recent advances in velocity estimations have been developed by Ji *et al.* (2003).

III. EXPERIMENTS AND RESULTS

In the validating experiments, two bending piezoelements known as bimorphs (Piezo Systems, Cambridge, MA) are applied as the vibration sources. A double channel signal generator (Tektronix AFG320) produces two monochrome low frequency signals at slightly different frequencies. A GE Logiq 700, which has been specially modified to implement the sonoelastography functions, is applied to visualize the "crawling wave" propagation. A schematic drawing of the experiment setup is depicted in Fig. 5.

A. Crawling wave experiments

Two experiments were conducted to validate the theory of crawling waves. First, a double-layer gelatin phantom was constructed. The hard layer of the phantom was made of 1000 g H_2O, 70 g gelatin (Knox™), 100 g glycerin, and 10 g graphite. The soft layer of the phantom was made of 1000 g H_2O, 49 g gelatin, 100 g glycerin, and 10 g graphite. The phantom was placed in such a position that the boundary

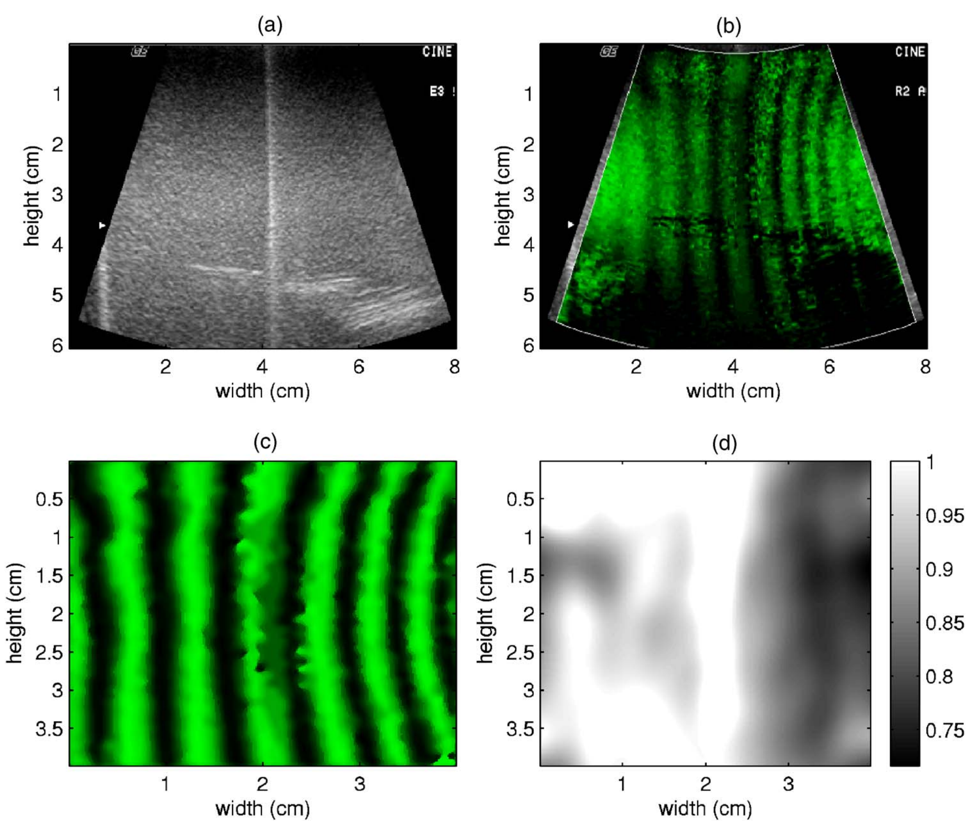

FIG. 6. Two-layer gelatin phantom experiment. (a) The B-mode ultrasound image of the phantom. The hard layer is on the left and the soft layer is on the right. (b) One frame of the crawling wave video taken with sonoelastography. The brightness of each pixel corresponds to the amplitude of the local vibration. Please note that the dc background is subtracted from the image for clarity. It can be seen that the crawling wave wavelength is larger in the left half of the phantom than that in the right half. (c) The cropped and enhanced sonoelastography image of the crawling waves with the amplitude information removed. (d) The normalized crawling wave speed estimation based on LFE algorithm.

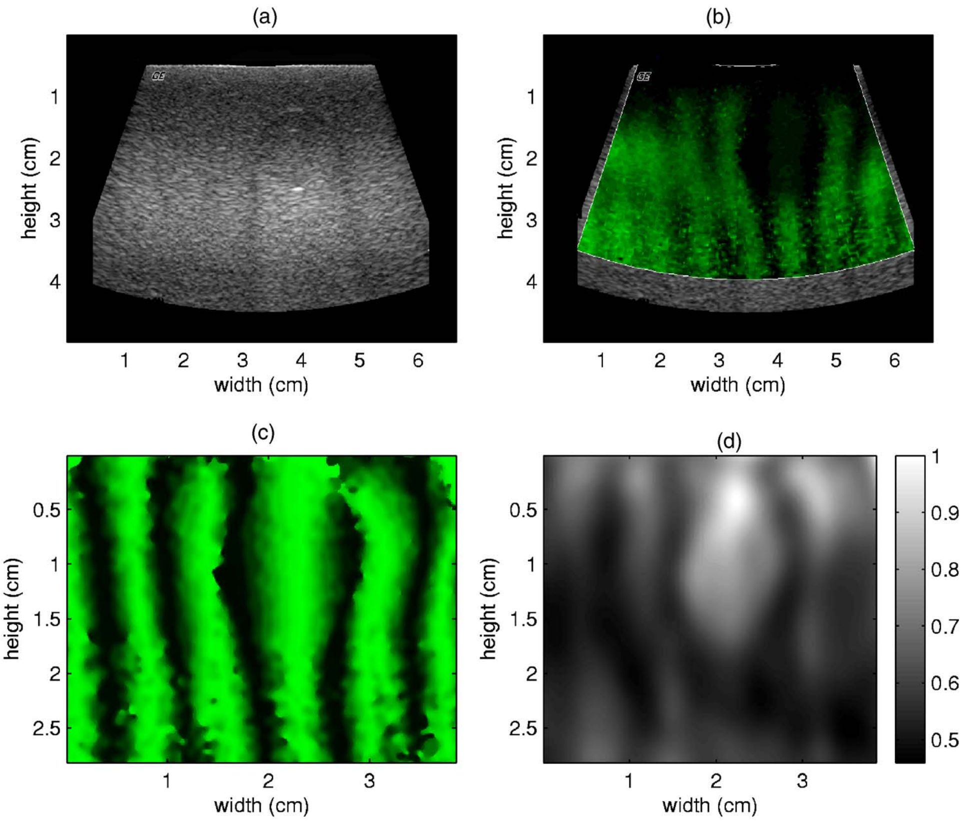

FIG. 7. Commercial (Zerdine) phantom experiment. (a) The B-mode ultrasound image of the phantom with a stiff inclusion. (b) One frame of the crawling wave video taken with sonoelastography. Please note that the dc background is subtracted from the image for clarity. It can be seen that the crawling wave wavelength is larger in the inclusion than outside. (c) The enhanced sonoelastography image with the amplitude information removed. (d) The normalized crawling wave speed estimation based on LFE algorithm.

of the two layers was vertical with the hard layer on the left and the soft layer on the right. The B-mode ultrasound image of the phantom is shown in Fig. 6(a).

The shear wave velocities of the hard and the soft layer of the phantom are estimated, respectively, with the method described in Wu *et al.* (2004). The estimated shear wave speed in the hard layer is 3.3 m/s. The estimated shear wave speed in the soft layer is 1.9 m/s.

The bimorphs are placed in close contact with the left side and the right side of the phantom. The two bimorphs vibrate at 300 and 300.2 Hz, respectively. The frequency difference $\Delta\omega$, namely, 0.2 Hz, was selected to achieve the best video quality with the Doppler frame rate (roughly seven frames per second). The shear wave interference pattern (one frame of the video) is shown in Fig. 6(b). It can be seen that the crawling wave wavelengths in the two layers are different. The wavelength in the hard half is longer and the wavelength in the soft half is shorter. The video sequence is cropped around the layer interface and enhanced by fitting the time trace at each pixel to a cosine curve [Fig. 6(c)]. The bank of LFE filters were applied on each of the 60 frames of the crawling wave video and the average of the outcome is shown in Fig. 6(d). The brightness of this image corresponds to the local crawling wave speed, which is inversely proportional to the local spatial frequency. The speed estimation was high (bright) in the hard layer and was low (dark) in the soft layer.

Moreover, a Zerdine tissue phantom (CIRS Norfolk, VA) is applied in the experiment. The phantom is bowl shaped and approximately $15 \times 15 \times 10$ cm in size. With the exception of a small spherical inclusion out of the imaging plane, the phantom is isotropic and homogeneous with uniform shear modulus. The tissue-mimicking material has a sound speed near 1540 m/sec. The background material has a Young's modulus of 20 KPa and a shear modulus of 6.67 KPa. The stiff spherical inclusion is 1.3 cm in diameter and approximately seven times as stiff as the background. A B-mode ultrasound image of the phantom is shown in Fig. 7(a). The inclusion is vaguely visible in the B-mode image. Two bimorphs are placed against the sides of the phantom, vibrating at 210 and 210.1 Hz, respectively. One frame of the crawling wave propagation video over the stiff lesion is shown in Fig. 7(b). The distortion of the crawling wave wave fronts around the stiff inclusion is visible. Because of the symmetry of the two sources, the distortions appear both before and after the lesion. The video is cropped around the lesion and enhanced by fitting the time trace at each pixel to a cosine curve Fig. 7(c). By applying the LFE upon each frame of the propagation video and taking the average of the outputs, we have an estimation of the crawling wave velocity distribution in the phantom, shown in Fig. 7(d). The brightness of Fig. 7(d) corresponds to the local shear wave speed, which is inversely proportional to the local spatial frequency. The region with high crawling wave speed agrees with the location of the stiff inclusion.

B. Holographic wave experiments

Similar experiments are performed with the holographic wave technique. One channel of the signals (199.9 Hz) drives a bending piezo elements known as Thunder (Face International Corporation, Norfolk, VA) which is applied to vibrate the US transducer. The other channel of the signal (200 Hz) drives a shear wave actuator (Piezo system, MA),

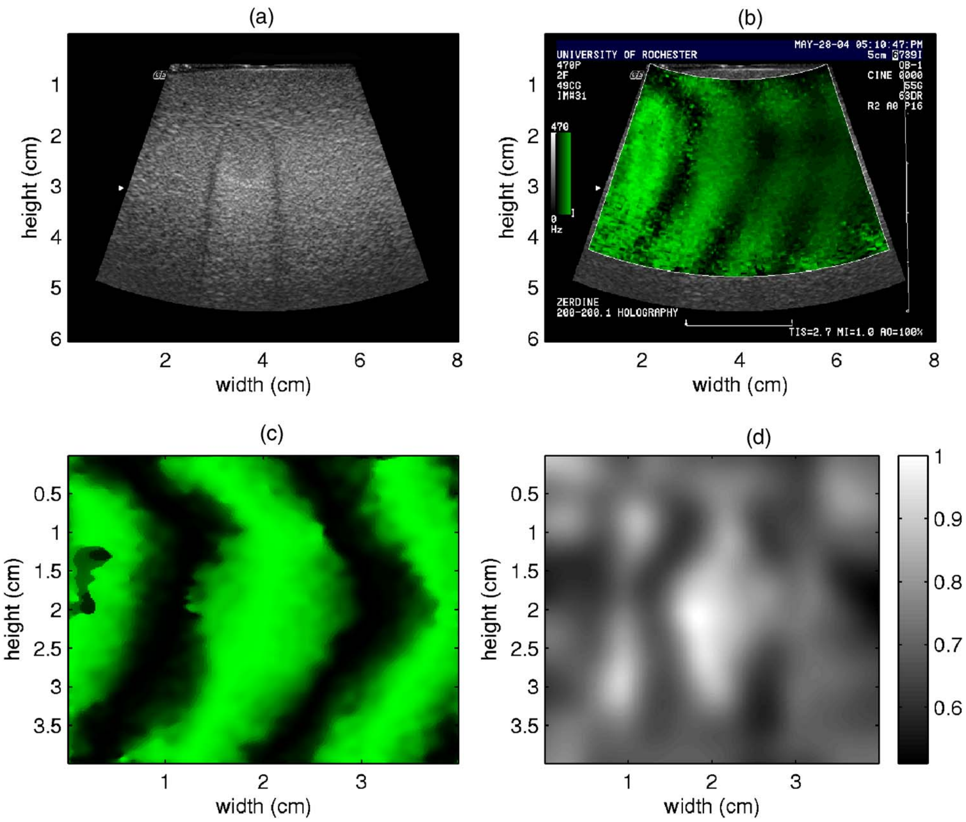

FIG. 8. (a) The B-mode ultrasound image of the phantom with a stiff inclusion. (b) One frame of the holography wave video taken with sonoelastography. It can be seen that the holography wave wavelength is larger in the inclusion than outside. (c) The enhanced sonoelastography image with the amplitude information removed. (d) The normalized holography wave speed estimation based on LFE algorithm.

which propagates shear waves into a Zerdine phantom. With the real-time visualization, the shear waves are virtually "slowed down" so that the local and subtle behaviors of the waves can be examined closely. The different wave speeds within and outside of the lesion can be perceived by human eye. One frame of the "modulation wave" propagation is shown in Fig. 8(b). The shear wave wave fronts are visibly distorted by the hard inclusion and thus the size and the location of the lesion may be estimated. One estimation of the stiffness distribution with LFE is shown in Fig. 8(d).

IV. DISCUSSION

In order for Eq. (10) ($\upsilon_{\text{pattern}}=\Delta\omega/2\omega\cdot\upsilon_{\text{shear}}/\cos(\theta/2)$) to be valid, we have to assume the medium is locally homogeneous, in other words, if there is an abrupt changes in the shear modulus, Eq. (A2) is not valid. Near the boundary of such abrupt changes, the assumption that $\cos(\theta)\approx 1$ in Eq. (A2) may not be valid either (The holographic wave does not require this condition). Therefore, the shear wave speed estimation close to the media boundary is not exact. A reasonable approximation of the size of the transition zone near the boundary is on the order of the wavelength of the crawling waves. Therefore, increasing the frequency of the crawling wave, thus reducing the wavelength, may increase the reconstruction resolution of the shear wave velocity. In particular, if the size of the lesion is less than the crawling wave wavelength, the shear wave speed in the whole lesion may be misestimated, thus the reconstructed shear wave speed may not exactly reflect the physical stiffness contrast. Also, the LFE filters' region of support plays a role in setting the lower limit of resolution. However, even in this case, the proposed technique is able to qualitatively indicate the location of the stiff region with reasonable estimation of its size and shape.

The theory of holographic wave requires fewer assumptions. The only major assumption is that the medium is linear so that no higher harmonics other than the input signal exist. However, due to the reduced signal strength beyond the obstacles, the holographic wave method provides less accurate estimation than the crawling wave method in the far field.

The accurate shear wave estimates partly depend on the signal strength. Estimation errors and imaging artifacts may occur in deep tissues or where ultrasound shadows occur. In such locations, sonoelastographic signals are too weak to present correct spatial frequency and may thus be estimated as high crawling/holographic speed regions. Similarly, regions close to the shear wave sources may saturate the sonoelastographic estimator and thus also present low spatial frequency.

Like many other imaging modalities, there exists a tradeoff between the estimation accuracy and the image resolution of either the crawling wave or the holographic wave reconstructions. The relation is formulated in Appendix B with a realistic example provided. This tradeoff exists because of the noisy nature of the signals and the finite size of US foci. Please note that this appendix intends to find the lower (finer) bound of the resolution without considering any particular estimator. This lower bound may not be achievable.

V. CONCLUSION

We developed two experimental procedures to induce and visualize the shear wave interference patterns in tissue mimicking soft materials in real time. The interference patterns caused by two shear wave sources or one wave source and vibrating U.S. transducer move at a certain speed, which is proved to be related to the local shear wave velocity. The local interference pattern speeds are estimated in both a two-layer gelatin phantom and a commercial phantom with a stiff inclusion. The shear wave velocity and thus the shear modulus of each phantom are therefore reconstructed off line. This technique provides a real-time visualization of crawling waves with quantitative assessment of local elastic properties.

ACKNOWLEDGMENTS

The authors are thankful to Professor Nicholas George for informative discussion. This work was supported in part by the NSF/NYS Center for Electronic Imaging Systems, NIH Grant No. 2 R01 AG16317-01A1, the University of Rochester Departments of Radiology and Electrical and Computer Engineering, and the General Electric Company (GE).

APPENDIX A: INTERFERENCE FRINGES IN 2-D SPACE

As drawn in Fig. 3, the wave front AB from the left source and the wave front CD from the right source intersects at O. For the sake of convenience, the interference pattern is redefined as *the set of intersection points of AB and CD as they evolve in time.*

Theorem 1. OP is the interior angle bisector of angle $\angle$AOD.

Proof. Suppose wave front AB and wave front CD intersect at O at time 0. After a short period of time, AB moves to $A'B'$ and CD moves to $C'D'$ and they intersect at O'. OO' is the local segment of the interference pattern, as drawn in Fig. 3. Since AB and CD move at the same speed $EO=OF=FO'=O'E$. Therefore, $\triangle OEO'$ and $\triangle OFO'$ are congruent. Hence, OO' divides $\angle AOD$ in equal halves. Since the source frequency difference does not change the orientation of the wave fronts nor the interference pattern at a particular location, this relation is valid for both the static interference pattern case, and the crawling wave case.

In Fig. 10, suppose the wave fronts are at AB and CD, respectively, at $t=0$ and the interference fringe is at OP. Then, after a small period of time, at $t=\Delta T$, AB advances to $A'B'$ with $k_l \cdot d=\omega \cdot \Delta T$. Should CD have the same frequency, it would advance to the dashed line $C''D''$. However, since CD has a slight different frequency, it advances to $C'D'$ instead with

$$d' \cdot k_l = \omega \cdot \Delta T + \Delta\omega \cdot \Delta T, \tag{A1}$$

where k_l is the local wave number of shear wave, and ΔT is an infinitesimal time interval.

It is easy to prove that without the frequency difference, $A'B'$ and $C''D''$ produce the same interference fringe OP. The frequency difference $\Delta\omega$, however, causes a fringe displacement from OP to $O'P'$.

The distance between CD and $C''D''$ is $d'-d=\Delta\omega \cdot \Delta t/k_l$. Let $\angle O'OD''$ be θ, then $|OO'|=(d'-d)/\sin(\theta)$.

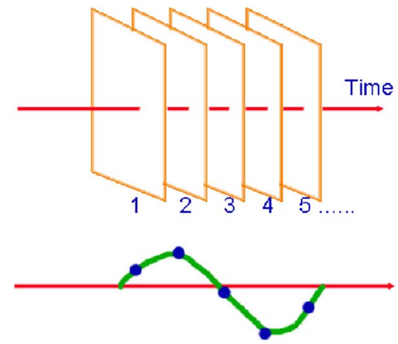

FIG. 9. Phase of the time trace of the pixel value of the hologram video is estimated.

The distance between OP and $O'P'$ is $d''=|OO'|*\sin(\theta/2)$, according to Theorem 1. So

$$d'' = \left| OO' \right| * \sin(\theta/2) = \frac{d'-d}{\sin(\theta)} * \sin(\theta/2) = \frac{d'-d}{2\cos\left(\frac{\theta}{2}\right)}$$

$$= \frac{\Delta\omega \cdot \Delta T}{2\cos\left(\frac{\theta}{2}\right)k} = \frac{\Delta\omega \cdot \Delta T \cdot v_{\text{shear}}}{2\omega\cos\left(\frac{\theta}{2}\right)}$$

$$\frac{d''}{\Delta T} = \frac{\Delta\omega \cdot v_{\text{shear}}}{2\omega\cos\left(\frac{\theta}{2}\right)}$$

$$v_{\text{pattern}} = \frac{\Delta\omega}{2\omega} \cdot \frac{v_{\text{shear}}}{\cos\left(\frac{\theta}{2}\right)}. \tag{A2}$$

Comparing Eq. (A2) with Eq. (9), we see that in the 2D domain, an extra factor of $1/\cos\left(\frac{\theta}{2}\right)$ is introduced. Other than this factor, the velocity of the interference pattern is solely dependent on the local shear wave velocity and the frequencies relation. We further notice that if the two shear wave sources are far separated comparing to the size of the ROI, $\theta/2$ is a small quantity and $\cos\left(\frac{\theta}{2}\right)$ is close to 1, thus

$$v_{\text{pattern}} \approx \frac{\Delta\omega}{2\omega} \cdot v_{\text{shear}}. \tag{A3}$$

APPENDIX B: ESTIMATOR ACCURACY CONSIDERATIONS

In the proceeding shear wave velocity estimation procedures, it is obvious that the final estimation results rely extensively upon the phase estimation of the local vibration. The local vibration phase is estimated by tracking the brightness variation at each pixel as shown in Fig. 9. In this appendix, the lower bound of the crawling/holographic wave velocity error is formulated and an example with realistic values is given.

According to Eq. (18), the modulation wave equation is

$$|P(x,t)|^2 = f(x)^2 + A^2 - 2A \cdot f(x)\cos[\Delta\omega t - s(x)].$$

At a given location x_o, the pixel value is

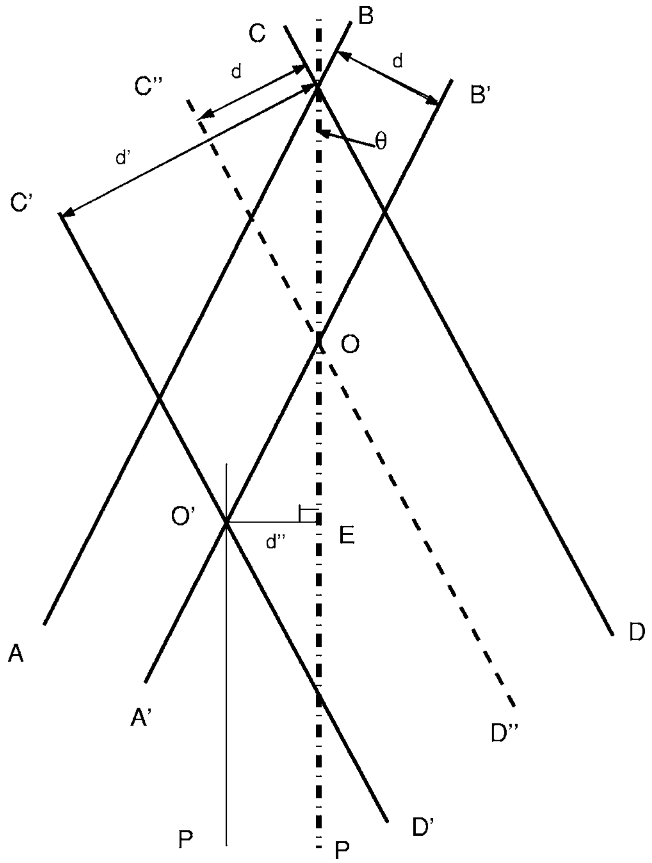

FIG. 10. The geometry of shear wave wavefronts in an infinitesimal region. The shear wave sources (not shown) are vibrating at slightly different frequencies.

$$B(t) = f(x_o)^2 + A^2 - 2A \cdot f(x_o)\cos[\Delta\omega t - s(x_o)]. \quad \text{(B1)}$$

Assume the signal is in white Gaussian noise, the discrete pixel value over multiple observations (multiple frames of the wave video) can be written as

$$x[n] = C + D \cdot \cos(\Delta\omega n + \phi) + w[n], \quad \text{(B2)}$$

where $C = f(x_o)^2 + A^2$, $D = -2A \cdot f(x)$, $\phi = -s(x_o)$, and $w(n) = \mathcal{N}(0, \sigma^2)$, a zero mean Gaussian distribution with standard deviation σ.

Therefore, the likelihood function is

$$p(x;\phi) = \frac{1}{(2\pi\sigma^2)^{\frac{N}{2}}} \cdot \exp\left[-\frac{1}{2\sigma^2} \sum_{n=0}^{N-1} \{x[n] - C - D \cdot \cos(\Delta\omega n + \phi)\} \right]. \quad \text{(B3)}$$

Taking the first and second derivatives of the natural logarithm of the likelihood function yields

$$\frac{\partial p(x;\phi)}{\partial \phi} = -\frac{1}{\sigma^2} \cdot \sum_{n=0}^{N-1} [x[n] - C - D \cdot \cos(\Delta\omega n + \phi)] \cdot D \sin(\Delta\omega n + \phi) \quad \text{(B4)}$$

and

TABLE I. Summary of the Major parameters to produce the point spread function simulation.

Parameter	Value
Sampling frequency	150e6 Hz
Speed of sound	1540 m/s
Central frequency	7.5e6 Hz
Relative Bandwidth	30%
Number of element	128
F number	3

$$\frac{\partial^2 p(x;\phi)}{\partial \phi^2} = -\frac{D}{\sigma^2} \cdot \sum_{n=0}^{N-1} [(x[n] - C) \cdot \cos(\Delta\omega n + \phi) - D\cos(2\Delta\omega n + 2\phi)]. \quad \text{(B5)}$$

Taking the negative expected value, we have

$$\begin{aligned} -E\left[\frac{\partial^2 p(x;\phi)}{\partial \phi^2}\right] &= \frac{D}{\sigma^2} \cdot \sum_{n=0}^{N-1} [(x[n] - C) \cdot \cos(\Delta\omega n + \phi) - D\cos(2\Delta\omega n + 2\phi)] \\ &= \frac{D}{\sigma^2} \cdot \sum_{n=0}^{N-1} [D\cos^2(\Delta\omega n + \phi) - D\cos(2\Delta\omega n + 2\phi)] = \frac{D^2}{\sigma^2} \cdot \sum_{n=0}^{N-1} \left[\frac{1}{2} + \frac{1}{2}\cos(2\Delta\omega n + 2\phi) - \cos(2\Delta\omega n + 2\phi)\right]. \end{aligned}$$

If we acquire integer or half integer number of cycles in experiments by choosing $\Delta\omega N = m\pi$, m being an integer, the expected value of the cos term is zero

$$E[\cos(2\Delta\omega n + 2\phi)] = 0. \quad \text{(B6)}$$

Thus,

$$-E\left[\frac{\partial^2 p(x;\phi)}{\partial \phi^2}\right] = \frac{ND^2}{2\sigma^2}. \quad \text{(B7)}$$

We notice that the inverse of Eq. (B7) gives the Cramer-Rao lower bound of the phase estimation

$$\mathrm{var}(\hat{\phi}) \geq \frac{1}{-E\left[\frac{\partial^2 p(x;\phi)}{\partial \phi^2}\right]} = \frac{2\sigma^2}{ND^2} \quad \text{(B8)}$$

The local shear wave velocity estimation is equivalent to estimating the local slope of the phase function. At this stage, the tradeoff of image resolution and estimation accuracy has to be considered. If we set the image resolution to be the size of M pixels, the accuracy of the slope estimation is bounded by a function of M. If we model the problem as a line fitting problem, and assume the phase function is in the form of

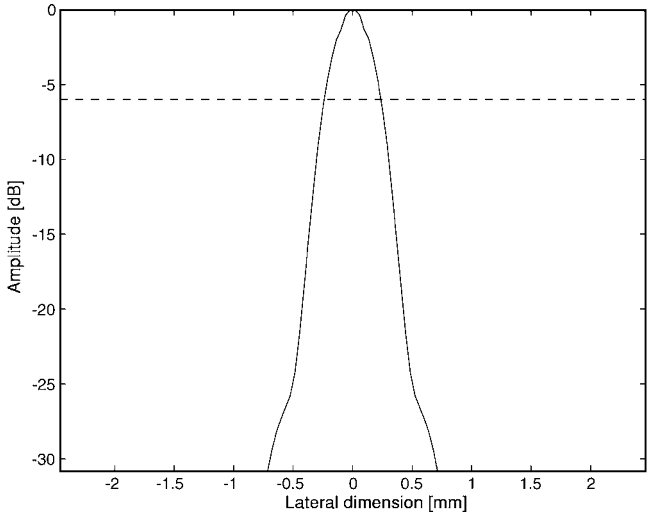

FIG. 11. $6dB$ width of the ultrasound scanner's point spread function simulated with Field II tool box.

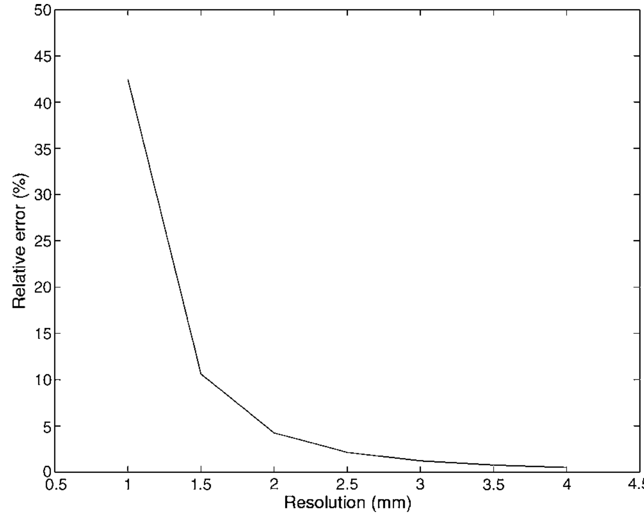

FIG. 12. The tradeoff between the image resolution and the relative error.

$$\phi[m] = F + G \cdot m + w[m], \tag{B9}$$

where $w[m]$ is a zero mean Gaussian distribution with variance determined by Eq. (B8). With the independent observations at these M pixels, we may obtain the slope estimation G with variance

$$\mathrm{var}(\hat{G}) \geq \frac{12 \cdot \mathrm{var}(\hat{\phi})}{M(M^2-1)}. \tag{B10}$$

Because the stiff regions are generally of more importance than the normal background, we pay more attention to the estimator accuracy in the stiff regions. The vibration amplitude is low in these regions due to the sonoelastography effect, the signal-to-noise ratio (SNR) is thus also low. An empirical estimate of the SNR in the stiff regions is 1. In our experiments, a typical number of frames of the shear wave propagation video is 60. Thus in Eq. (B8), the variance of the phase estimation is approximately $1/30$.

M in Eq. (B10) refers to the number of independent measurements. The ultrasound scanner determines that only one independent measurement can be made within the width of the point spread function. A point spread function is simulated with the Field II tool box Jensen and Svendsen 1992. The imaging system parameters are selected from a typical experiment setting and are summarized in Table I.

The simulation shows that the 6 dB width of the point spread function in the lateral direction is approximately 0.5 mm (Fig. 11). Assuming a realistic shear wave speed of 4 m/s and a driving frequency at 200 Hz, we proceed to discuss the relation between the elasticity estimation resolution and the estimation relative error.

Assume that we choose the resolution to be 2 mm, then there are four independent measurements within this length. According to Eq. (B10)

$$\mathrm{var}(\hat{G}) \geq \frac{12 \cdot \mathrm{var}(\hat{\phi})}{M(M^2-1)} = \frac{12 \cdot 1/30}{4(4^2-1)} = 0.0067. \tag{B11}$$

Since the phase increase is 2π over one shear wave wavelength, the phase slope may be estimated by

$$\mathrm{slope}_{\phi} = 2\pi/\lambda = 2\pi/(20 * 2) = 0.1571. \tag{B12}$$

Thus the relative error is 4%.

The tradeoff between the elasticity image resolution and the estimation relative error is plotted in Fig. 12. Please note that Eq. (B10) provides a lower bound of the estimation accuracy. In practice, this lower bound may not be achievable.

Braun, J., Buntkowsky, G., Bernarding, J., Tolxdorff, T., and Sack, I. (**2001**). "Simulation and analysis of magnetic resonance elastography wave images using coupled harmonic oscillators and gaussian local frequency estimation," Magn. Reson. Imaging **19**, 703–713.

Bishop, J., Samani, A., Sciarretta, J., and Plewes, D. B. (**2000**). "Two-dimensional mr elastography with linear inversion reconstruction: methodology and noise analysis," Phys. Med. Biol. **45**, 2081–2091.

Catheline, S., Wu, F., and Fink, M. (**1999**). "A solution to diffraction biases in sonoelasticity: the acoustic impulse technique," J. Acoust. Soc. Am. **105**, 2941–2950.

Dutt, V., Kinnick, R. R., Muthupillai, R., Oliphant, T. E., Ehman, R., and Greenleaf, J. F. (**2000**). "Acoustic shear-wave imaging using echo ultrasound compared to magnetic resonance elastography," Ultrasound Med. Biol. **26**, 397–403.

Dutt, V., Manduca, A., Muthupillai, R., Ehman, R., and Greenleaf, J. (**1997**). "Inverse approach to elasticity reconstruction in shear wave imaging," *Proceeding of IEEE Ultrasonics Symposium* Vol. **2**, pp. 1415–1418.

Greenleaf, J. F., Fatemi, M., and Insana, M. (**2003**). "Selected methods for imaging elastic properties of biological tissues," Annu. Rev. Biomed. Eng. **5**, 57–78.

Huang, S. R., Lerner, R. M., and Parker, K. J. (**1990**). "On estimating the amplitude of harmonic vibration from the doppler spectrum of reflected signals," J. Acoust. Soc. Am. **88**, 2702–2712.

Huang, S. R., Lerner, R. M., and Parker, K. J. (**1992**). "Time domain Doppler estimators of the amplitude of vibrating targets," J. Acoust. Soc. Am. **91**, 965–974.

Jenkyn, T. R., and Ehman, R. L., "An KN 2003 Noninvasive muscle tension measurement using the novel technique of magnetic resonance elastography (MRE)," J. Biomech. **36**, 1917–1921.

Jensen, J. A., and Svendsen, N. B. (**1992**). "Calculation of pressure fields from arbitrarily shaped, apodized, and excited ultrasound transducers," IEEE Trans. Ultrason. Ferroelectr. Freq. Control **39**, 262–267.

Ji, L., and McLaughlin, J. (**2004**). "Recovery of the lame parameter mu in biological tissues," Inverse Probl. **20**, 1–24.

Ji, L., McLaughlin, J. R., Renzi, D., and Yoon, J. R. (**2003**). "Interior elastodynamics inverse problems: Shear wave speed reconstruction in transient elastography," Inverse Probl. **19**, 1–29.

Knutsson, H., Westin, C. J., Granlund, G. (**1994**). "Local multiscale frequency and bandwidth estimation," *Proc. IEEE Intl Conf on Image Processing*, Vol. **1**, pp. 36–40.

Lerner, R. M., Parker, K. J., Holen, J., Gramiak, R., and Waag, R. C. (**1988**).

"Sono-elasticity: Medical elasticity images derived from ultrasound signals in mechanically vibrated targets," Acoustical Imaging. Vol. **16**. *Proceedings of The 16th International Symposium*, pp. 317–327.

Levinson, S. F., Shinagawa, M., and Sata, T. (**1995**). "Sonoelastic determination of human skeletal-muscle elasticity," J. Biomech. **28**, 1145–1154.

Love, A. E. H. (**1944**). *A Treatise on the Mathematical Theory of Elasticity* (Dover, New York), Chap. 13.

Manduca, A., Dutt, V., Borup, D. T., Muthupillai, R., Ehman, R. L., and Greenleaf, J. F. (**1998**). "Reconstruction of elasticity and attenuation maps in shear wave imaging: An inverse approach," *Medical Image Computing and Computer-assisted Intervention-Miccai'98*, pp. 606–613.

Manduca, A., Muthupillai, R., Rossman, P. J., Greenleaf, J. F., Ehman, R. L. (**1996**). "Image processing for magnetic resonance elastography," Proc. SPIE **2710**, 616–623.

Manduca, A., Oliphant, T. E., Dresner, M. A., Mahowald, J. L., Kruse, S. A., Amromin, E., Felmlee, J. P., Greenleaf, J. F., and Ehma, R. L., (**2001**). "Medical image analysis: Non-invasive mapping of tissue elasticity," Antivir. Chem. Chemother. **5**, 237–254.

Muthupillai, R., Lomas, D. J., Rossman, P. J., Greenleaf, J. F., Manduca, A., and Ehman, R. L. (**1995**). "Magnetic-resonance elastography by direct visualization of propagating acoustic strain waves," Science **269**, 1854–1857.

Oliphant, T. E., Kinnick, R. R., Manduca, A., Ehman, R. L., Greenleaf, J. F. (**2000**). "An error analysis of helmholtz inversion for incompressible shear, vibration elastography with application to filter-design for tissue characterization," *Ultrasonics Symposium, 2000 IEEE*, Vol. **2**, pp. 1795–1798.

Parker, K. J., Huang, S. R., Musulin, R. A., and Lerner, R. M. (**1990**). "Tissue-response to mechanical vibrations for Sonoelasticity imaging," Ultrasound Med. Biol. **16** (3) 241–246.

Parker, K. J., and Lerner, R. (**1992**). "Shear waves ring a bell," J. Ultrasound Med. **11**, 387–392.

Sandrin, L., Catheline, S., Tanter, M., Hennequin, X., and Fink, M. (**1999**). "Time-resolved pulsed elastography with ultrafast ultrasonic imaging," Ultrason. Imaging **21**, 259–272.

Taylor, L. S., Porter, B. C., Rubens, D. J., and Parker, K. J. (**2000**). "Three-dimensional sonoelastography: Principles and practices," Phys. Med. Biol. **45**, 1477–1494.

Wu, Z., Lawrance, T. S., Rubens, D. J., and Parker, K. J. (**2004**). "Sonoelastographic imaging of interference patterns for estimation of the shear velocity of homogeneous biomaterials," Phys. Med. Biol. **49**, 911–922.

Wu, Z., Taylor, L. S., Rubens, D. J., Parker, K. J. (**2002**). "Shear wave focusing for three-dimensional sonoelastography," J. Acoust. Soc. Am. **111**, 439–446.

Yamakoshi, Y., and Sato, J., and Sato, T. (**1990**). "Ultrasonic imaging of internal vibrations of soft tissue under forced vibration," IEEE Trans. Ultrason. Ferroelectr. Freq. Control **37**, 45–53.